

# Nowcast3D: Reliable precipitation nowcasting via gray-box learning

Huaguan Chen<sup>1</sup>, Wei Han<sup>2,3\*</sup>, Haofei Sun<sup>4</sup>, Ning Lin<sup>1</sup>, Xingtao Song<sup>5</sup>, Yunfan Yang<sup>6,7</sup>, Jie Tian<sup>2,8</sup>, Yang Liu<sup>9</sup>, Ji-Rong Wen<sup>1,10</sup>, Xiaoye Zhang<sup>3,11</sup>, Xueshun Shen<sup>2,3</sup>, Hao Sun<sup>1,10\*</sup>

<sup>1</sup>Gaoling School of Artificial Intelligence, Renmin University of China, Beijing, China

<sup>2</sup>Earth System Modeling and Prediction Center, China Meteorological Administration, Beijing, China

<sup>3</sup>State Key Laboratory of Severe Weather Meteorological Science and Technology, Beijing, China

<sup>4</sup>Shanghai Typhoon Institute, China Meteorological Administration, Shanghai, China

<sup>5</sup>School of Atmospheric Physics, Nanjing University of Information Science and Technology, Nanjing, China

<sup>6</sup>State Key Laboratory of Atmospheric Boundary Layer Physics and Atmospheric Chemistry, Institute of Atmospheric Physics, Chinese Academy of Sciences, Beijing, China

<sup>7</sup>College of Earth and Planetary Sciences, University of Chinese Academy of Sciences, Beijing, China

<sup>8</sup>Chinese Academy of Meteorological Sciences, China Meteorological Administration, Beijing, China

<sup>9</sup>School of Engineering Science, University of Chinese Academy of Sciences, Beijing, China

<sup>10</sup>Beijing Key Laboratory of Research on Large Models and Intelligent Governance, Beijing, China

<sup>11</sup>Laboratory of Climate Change Mitigation and Carbon Neutrality, Henan University, Zhengzhou, China

\*Corresponding authors

## Abstract

Extreme precipitation nowcasting demands high spatiotemporal fidelity and extended lead times, yet existing approaches remain limited. Numerical Weather Prediction (NWP) and its deep-learning emulations are too slow and coarse for rapidly evolving convection, while extrapolation and purely data driven models suffer from error accumulation and excessive smoothing. Hybrid 2D radar-based methods discard crucial vertical information, preventing accurate reconstruction of height-dependent dynamics. We introduce a gray-box, fully three-dimensional nowcasting framework that directly processes volumetric radar reflectivity and couples physically constrained neural operators with data driven learning. The model learns vertically varying 3D advection fields under a conservative advection operator, parameterizes spatially varying diffusion, and introduces a Brownian-motion-inspired stochastic term to represent unresolved motions. A residual branch captures small-scale convective initiation and microphysical variability, while a diffusion-based stochastic module estimates uncertainty. The framework achieves more accurate forecasts up to three-hour lead time across precipitation regimes and ranked first in 57% of cases in a blind evaluation by 160 meteorologists. By restoring full 3D dynamics with physical consistency, it offers a scalable and robust pathway for skillful and reliable nowcasting of extreme precipitation.

**Keywords:** Deep Learning, Nowcasting, 3D volumetric radar reflectivity, Physics-guided

## Introduction

On 16 June 2024, extreme rainfall struck multiple locations in Meizhou, Guangdong Province; ensuing floods and landslides in Pingyuan County, Jiaoling County and Meixian District drove sev-

eral rivers above historical levels, affected more than 160,000 people across eight administrative regions, and left 55 individuals dead or missing. Such episodes starkly illustrate the threat that intense precipitation poses to life and infrastructure, and they underscore the urgent need for nowcasting systems that deliver both longer lead times and higher spatiotemporal fidelity to enable timely warnings and risk mitigation.

Accurate short-term precipitation forecasts are central to disaster preparedness, yet extreme rainfall is inherently multiscale and fast evolving, placing severe demands on existing forecasting paradigms [1]. Weather radar offers a uniquely informative observational basis: modern networks produce volumetric reflectivity fields with horizontal resolutions approaching  $0.01^\circ$  ( $\approx 1$  km), minute-scale temporal sampling and vertical sampling on the order of hundreds of metres, yielding dense, three-dimensional measurements of precipitating structure and evolution [2–4]. Because reflectivity closely tracks instantaneous precipitation intensity, volumetric radar sequences encode both the advective imprint of the flow and vertical structure—echo-top variability, bright bands and layer-dependent reflectivity—that strongly modulate convective growth and propagation [5, 6].

Numerical weather prediction (NWP) remains indispensable from synoptic to subseasonal scales because it evolves the governing equations of motion and thermodynamics; however, operational NWP systems are constrained by update cycles, domain size and computational cost, which limit temporal refresh and spatial resolution and reduce their utility for minute-scale, high-resolution nowcasting of rapidly developing convection [7]. Deep learning efforts to accelerate or emulate NWP have improved speed and scalability [8–14], but they often inherit mesoscale grid spacing and hourly cadences from their training targets and therefore fall short of minute-scale convective nowcasting requirements. Complementary extrapolation techniques that advect recent fields using estimated motion (for example, pySTEPS) partially preserve advective conservation and can be skillful at short lead times, yet they accumulate positional and intensity drift with increasing lead time [15]. End-to-end data driven models trained on large radar archives have advanced spatiotemporal representation learning [16–20], but purely data driven forecasts commonly blur and attenuate extreme, small-scale convective features, undermining reliability for hazard-critical applications.

Hybrid, physics informed neural approaches have shown promise [21]. They aim to bridge the gap by embedding evolution operators or learned velocity fields into network architectures (for example, NowcastNet), thereby constraining forecasts with transport dynamics and improving realism in many cases [1]. Yet important limitations remain. Many hybrid methods operate on two dimensional radar composites (commonly the vertical maximum reflectivity, MAX(Z)), which discard vertical information and thus cannot represent height-dependent shear, inter-layer differential motion or echo-top evolution that are central to numerous convective and frontal processes [2, 3]. Moreover, attempts to estimate sparse 3D velocity fields directly are vulnerable to errors in the inferred motion and to the underdetermined nature of velocity recovery from reflectivity alone.

To overcome these limitations, we propose a unified three dimensional nowcasting framework that directly leverages volumetric radar reflectivity to jointly model coherent advection and localized stochastic dispersion. Instead of directly recovering a sparse 3D velocity field, we reconstruct the motion through a Helmholtz decomposition into stream and potential function components [22–24]. To represent local condensation and diffusion processes, we parameterize spatially varying diffusion strengths and incorporate a Brownian-motion-inspired stochastic term to account for unresolved residual motions, explicitly modeling hydrometeor dispersion beyond pure advection. Semi-Lagrangian advection [1, 25] combined with the stochastic term captures fluid like deformation and small scale dispersion, while unresolved microphysical and convective perturbations are handled by a learned residual branch. Building on this physics-grounded deterministic core, we integrate two complementary conditional diffusion modules [26–29]: one for large-scale structural evolution and the other for modeling residual, scale-localized variability. This decomposition provides a principled

pathway for ensemble forecasting and uncertainty representation [30]. In a systematic evaluation involving 160 professional meteorologists across China, over half of the participants expressed a clear preference for our approach over existing alternatives.

## Nowcast3D

We present Nowcast3D, a deep learning framework for volumetric radar reflectivity forecasting. At its core, the framework decomposes complex atmospheric processes into physically interpretable components, employing a hybrid architecture that synergistically integrates deterministic physical extrapolation with probabilistic generative modeling.

The methodology is founded on the decomposition of radar reflectivity evolution into three dominant physical processes: advection, the transport of hydrometeors by the three-dimensional wind field; local subgrid diffusion, representing small-scale turbulent mixing; and the microphysical tendency, which comprises in situ mass and phase changes (Figure 1a) [31]. This decomposition yields a compact and interpretable description of reflectivity dynamics, establishing a powerful prior for the deterministic component of Nowcast3D. The architecture comprises two tightly coupled stages (Figure 1b): a physics-driven prediction module and a probabilistic generation module. The physics-driven module first generates a single, coherent, and dynamically constrained deterministic forecast. Subsequently, the generative module uses this forecast as a basis to generate a full ensemble of plausible future states, capturing the inherent uncertainty of precipitation evolution.

The physics-driven module (Figure 1c) extrapolates the radar field by using a neural network to infer the governing physical processes from a sequence of past observations. In a single forward pass, a neural encoder processes the historical 3D radar states to directly output the complete spacetime fields for advection, local diffusion, and a residual source term across the entire forecast horizon. To address the vertical sparsity and heterogeneity inherent in volumetric radar data, one component infers the underlying motion, which is then processed through a Potential-Stream Function Decomposition to reconstruct a complete and dynamically consistent velocity field. Concurrently, other components infer a spatially varying, anisotropic diffusivity tensor and the source term representing the net effect of microphysical processes. As shown in Equation 5, the final deterministic forecast is then generated by solving the physical system defined by these three operators, using the last observed radar state as the initial condition and the network-inferred fields as the governing parameters. The detailed architecture of the model is provided in Extended Data Figure 1.

The probabilistic refinement stage is performed by a conditional diffusion model with a dual-branch architecture (Figure 1d). This design allows the model to separately generate the structural and intensity components of the forecast. The first branch is conditioned on both past radar observations and the deterministic forecast to generate the overall spatio-temporal structure of a plausible future state. Concurrently, the second branch is conditioned on the deterministic forecast and generates a field representing stochastic variations in precipitation intensity. The outputs from these two generative streams are then additively combined to produce a single, complete, and physically consistent ensemble member. As shown in Equation 7, by drawing multiple independent noise samples and passing them through the conditioned generative model, we produce a multi-member ensemble forecast that provides a principled quantification of forecast uncertainty. The detailed network architecture of the diffusion model is provided in Extended Data Figure 2.

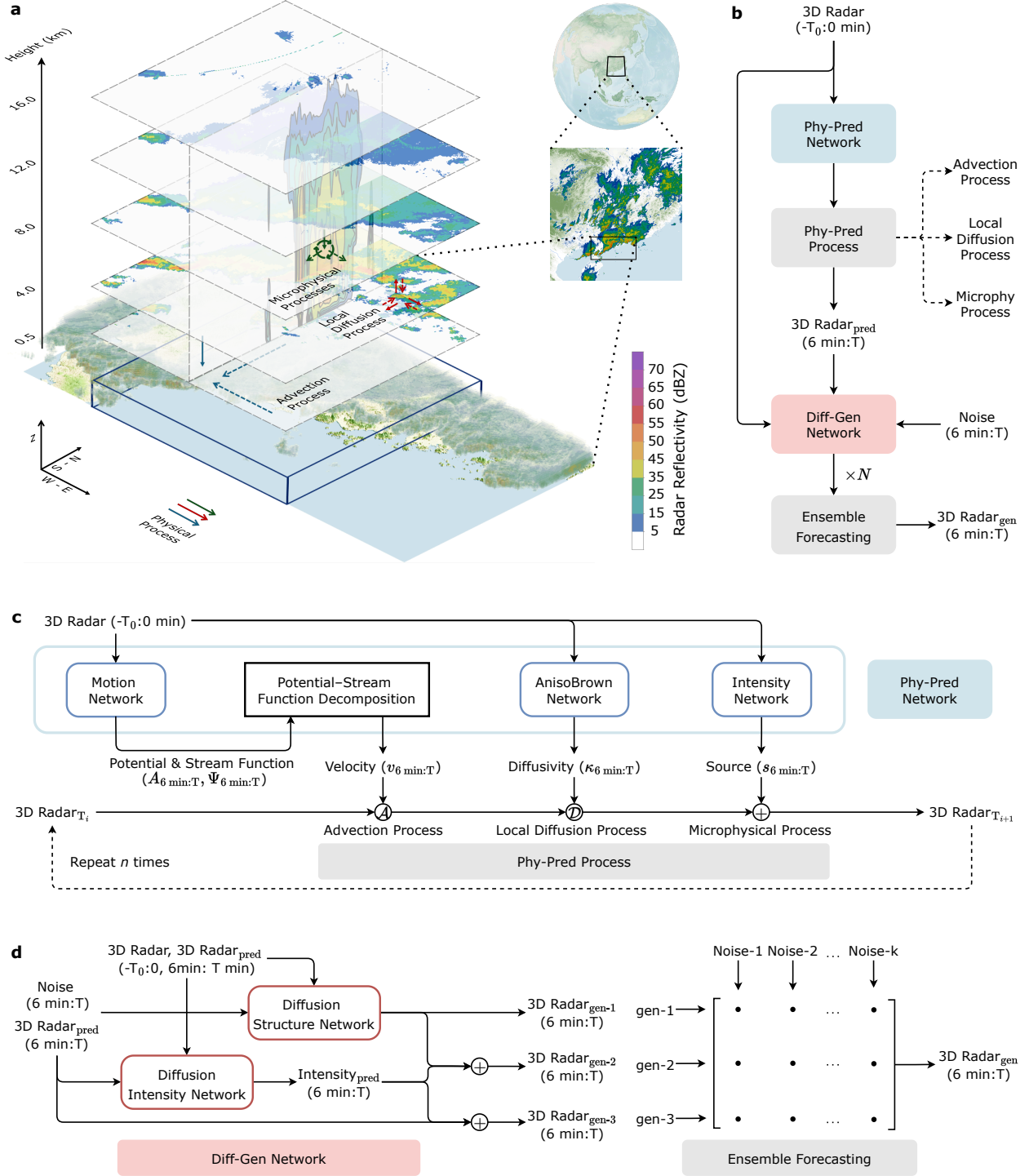


**Figure 1:** (a) Physical decomposition of reflectivity evolution. Reflectivity changes are partitioned into three contributions: advection by the 3D wind field, local diffusion representing small-scale spreading, and microphysical tendencies that alter reflectivity in situ. (b) Overall model schematic. Phy-Pred Network first infers latent physical fields from 3D radar; a physics-based predictor then evolves the three processes above. The physics forecast conditions a conditional diffusion model, and multiple independent noise samples produce an ensemble of probabilistic forecasts. (c) Deterministic physics backbone. The deterministic predictor inserts explicit advection, diffusion and microphysical operators into each temporal update. (d) The diffusion model captures physics-scale structure and stochastic residuals; varying noise trajectories under fixed conditioning produce calibrated probabilistic forecasts.

## Evaluation settings

We assess the predictive skill and operational utility of Nowcast3D against strong baselines representative of physics based, hybrid, and purely data driven nowcasting. The operational convective extrapolation system pySTEPS [15] serves as a physics informed reference widely adopted by national meteorological services. NowcastNet [1] couples physics informed priors with generative modeling and has demonstrated expert-validated operational value. SimVP [19], originally designed for video prediction, is included as a competitive deep learning baseline. Additional comparisons to PredRNN [17] and Earthformer [18] are provided in the Appendix.

All models were trained and evaluated on a large-scale corpus of radar observations from China. The training dataset comprises fixed-length sequences from South China during 2024, a region selected for its diverse convective regimes. To assess generalization, we conducted a rigorous cross-regional evaluation on an independent test set from North China, which has no geographical overlap with the training data. Furthermore, to evaluate performance in high resolution urban applications, we performed a specialized assessment on data from Maoming during 2025 at a  $0.01^\circ$  spatial resolution, enabling street level verification. Nowcast3D was trained on native volumetric (3D) radar data, while all 2D baseline models were trained on the column-maximum reflectivity derived from the same volumes to ensure a fair comparison. Across all experiments, models shared identical input output horizons and processing pipelines. Hyperparameters for all learning based models were tuned on a dedicated validation set, with the best performing checkpoint used for testing. No external data were used.

Our evaluation framework employs a set of three complementary metrics to jointly assess forecast quality. First, to assess location aware detection accuracy, we use the neighborhood Critical Success Index (CSI) [32], which quantifies event detection with spatial tolerance by counting hits, misses, and false alarms within prescribed radii at multiple reflectivity thresholds. Second, to diagnose the realism of predicted precipitation structures across different spatial scales, we analyze the Power Spectral Density (PSD) [33], comparing the power ratios and spectral slopes of forecasts against observations from convective to mesoscale ranges. Third, to measure perceptual similarity and structural fidelity, we employ the Learned Perceptual Image Patch Similarity (LPIPS) metric [34], which was computed on 2D column-maximum projections for equitable comparison with 2D baselines.

Beyond standard reflectivity based metrics, the unique ability of Nowcast3D to reconstruct the underlying atmospheric motion allows for direct physical validation. Accordingly, we independently verified the predicted three dimensional wind fields against co-located measurements from wind profiler radars and ground based weather stations across multiple altitudes.

## Large-scale forecast at $0.04^\circ$ resolution

We assess model performance on the extreme rainfall event that struck Beijing on 28 July 2025. This event prompted the Beijing Meteorological Observatory to issue a red heavy rain warning, the highest tier in China’s system, and ultimately resulted in substantial societal impact, including 30 reported fatalities. Our analysis focuses on the period of intense convection, between 15:00 and 18:00 UTC, during which the storm underwent rapid and complex structural evolution (Figure 2a).

The storm system was composed of two primary convective cells. A western cell propagated eastward, producing moderate but widespread precipitation. In contrast, the eastern cell was consistently the principal hazardous core, maintaining high intensity. Its evolution was highly non-linear. As the system propagated southeastward, it underwent significant consolidation and

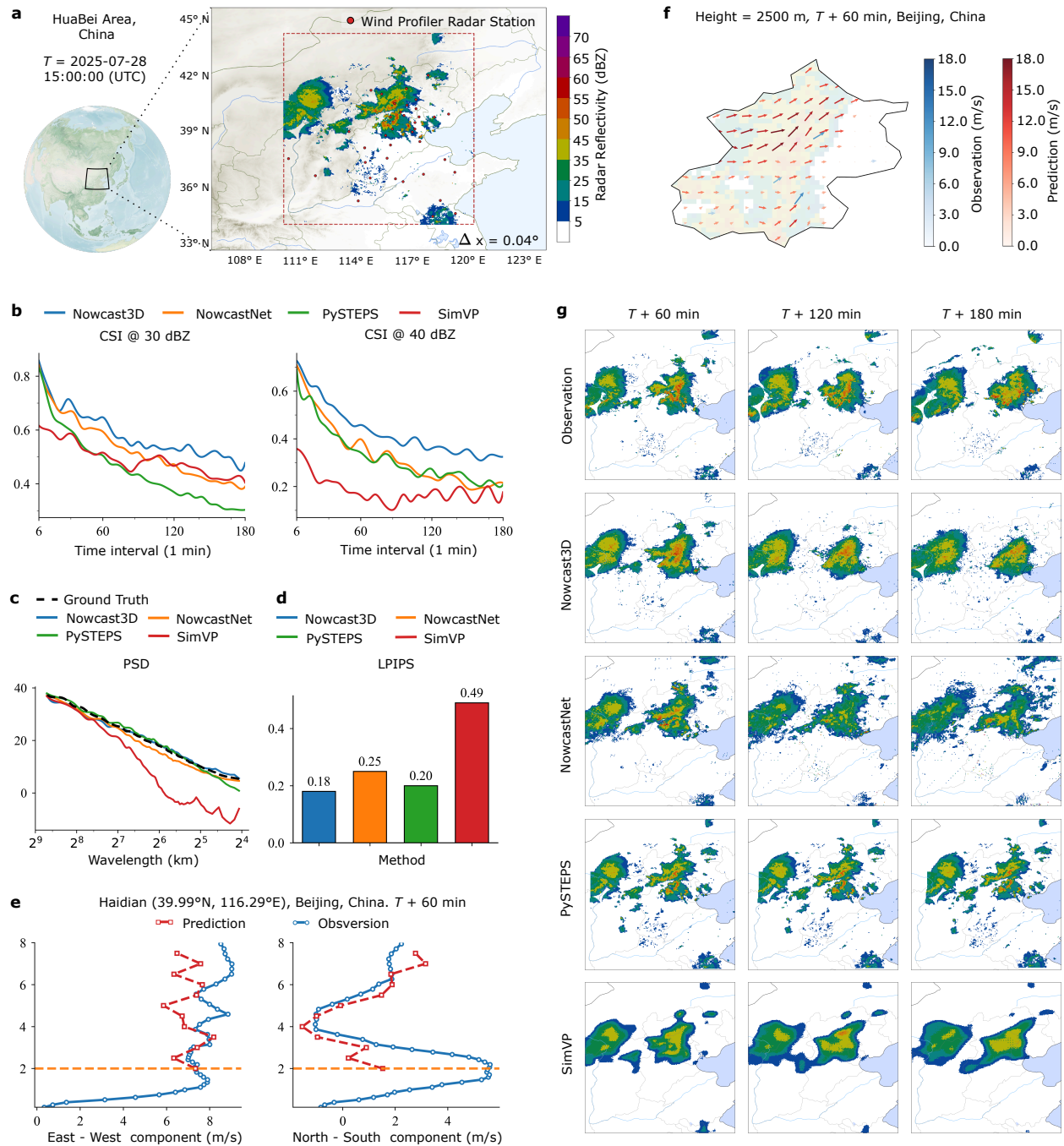


**Figure 2: Nowcast3D accurately forecasts the evolution of a severe mesoscale convective system.** **a**, Radar reflectivity of the convective system over North China at the forecast initialization time. The black box indicates the forecast domain, and red dots mark the locations of wind profiler radar stations. **b**, Quantitative forecast skill comparison using the CSI at 30 dBZ and 40 dBZ reflectivity thresholds over the 3 hour forecast horizon. **c**, Analysis of spatial scale fidelity using PSD. Forecast spectra are compared to the observed spectrum (black dashed line). **d**, Perceptual similarity assessment using the LPIPS metric. Lower values indicate better performance. **e**, Vertical wind profile validation at the Haidian station. The predicted zonal (east–west) and meridional (north–south) wind components are compared against wind profiler observations at 60 minute. **f**, Comparison of the predicted horizontal wind field with wind profiler observations in Beijing at an altitude of 2,500 m, 60 minutes into the forecast. **g**, Visual comparison of forecast reflectivity fields from Nowcast3D and baseline models against the observed radar sequence.

organization. Within this consolidating system, the region of extreme precipitation formed a distinct V-shape. This internal structure was then characterized by strong differential kinematics: its eastern flank propagated eastward, while its southwestern flank moved toward the southwest and subsequently stalled. This complex evolution posed two critical forecasting challenges: first, predicting the intricate morphological changes arising from this differential motion, and second, realistically maintaining the high precipitation intensity without artificial dissipation.

A comparison of the predicted spatio-temporal evolution against the observed radar sequence reveals distinct performance differences. (Figure 2g). The forecast from SimVP exhibits rapid intensity decay and significant morphological distortion. While pySTEPS and NowcastNet better preserve reflectivity magnitudes and sharp structural features, they demonstrate substantial positional errors, failing to accurately represent the evolution of the hazardous eastern cell. In contrast, Nowcast3D accurately captures the storm’s complex evolution, successfully tracking the displacement of the eastern cell while preserving its structural integrity and intensity.

These qualitative observations are substantiated by quantitative metrics. Forecasts from Nowcast3D achieve consistently superior scores in neighborhood Critical Success Index (CSI) across all lead times, indicating a higher accuracy in predicting the location of heavy rainfall (Figure 2c). Furthermore, superior performance in both Learned Perceptual Image Patch Similarity (LPIPS) and Power Spectral Density (PSD) analysis confirms that forecasts from Nowcast3D achieve a higher degree of perceptual realism and more accurately represent the storm’s scale-dependent variability compared to all baseline models (Figure 2d).

A key capability of our framework is its ability to infer the internal three-dimensional wind field. To validate this physical component, we compared the predicted winds with independent observations from wind profiler radars. Figure 2f shows the predicted horizontal wind field at an altitude of 2,500 m over Beijing, 60 minutes into the forecast, which aligns well with co-located profiler measurements. Figure 2e further presents the vertical wind profiles at the Haidian station. The forecast successfully captures both the zonal (east–west) and meridional (north–south) wind structures. For the zonal wind, the model shows some deviation in trend but maintains consistent magnitude, while for the meridional wind, the trend agreement is stronger. These results demonstrate the model’s capability to reconstruct physically consistent wind fields. A comparison of the 3D layered predictions is presented in Extended Data Figure 3.

It is important to note that the inferred velocity field tracks the motion of hydrometeors and is therefore most reliable in regions with significant radar reflectivity. The accuracy of the wind field is inherently limited in areas devoid of precipitation or where low-altitude radar observations are sparse. Nevertheless, by providing a dynamically consistent, high resolution wind field within the precipitating volume, this approach serves as a valuable complement to the spatially sparse measurements from ground based stations. The calculation and comparison of the wind field are detailed in Extended Data Figure 5.

## Medium-scale forecast at $0.01^\circ$ resolution

To assess the model’s ability to generalize to finer spatial scales—a critical requirement for urban and operational forecasting—we evaluated its performance on an extreme precipitation event in Maoming on 16 August 2025. For this analysis, we evaluated all models on the event at a  $0.01^\circ$  spatial resolution (Figure 3a). This increase in resolution presents a formidable forecasting challenge, as it resolves faster, more complex atmospheric processes not explicitly represented in the coarser resolution training data.

The storm’s evolution was characterized by the eastward propagation of two primary convective

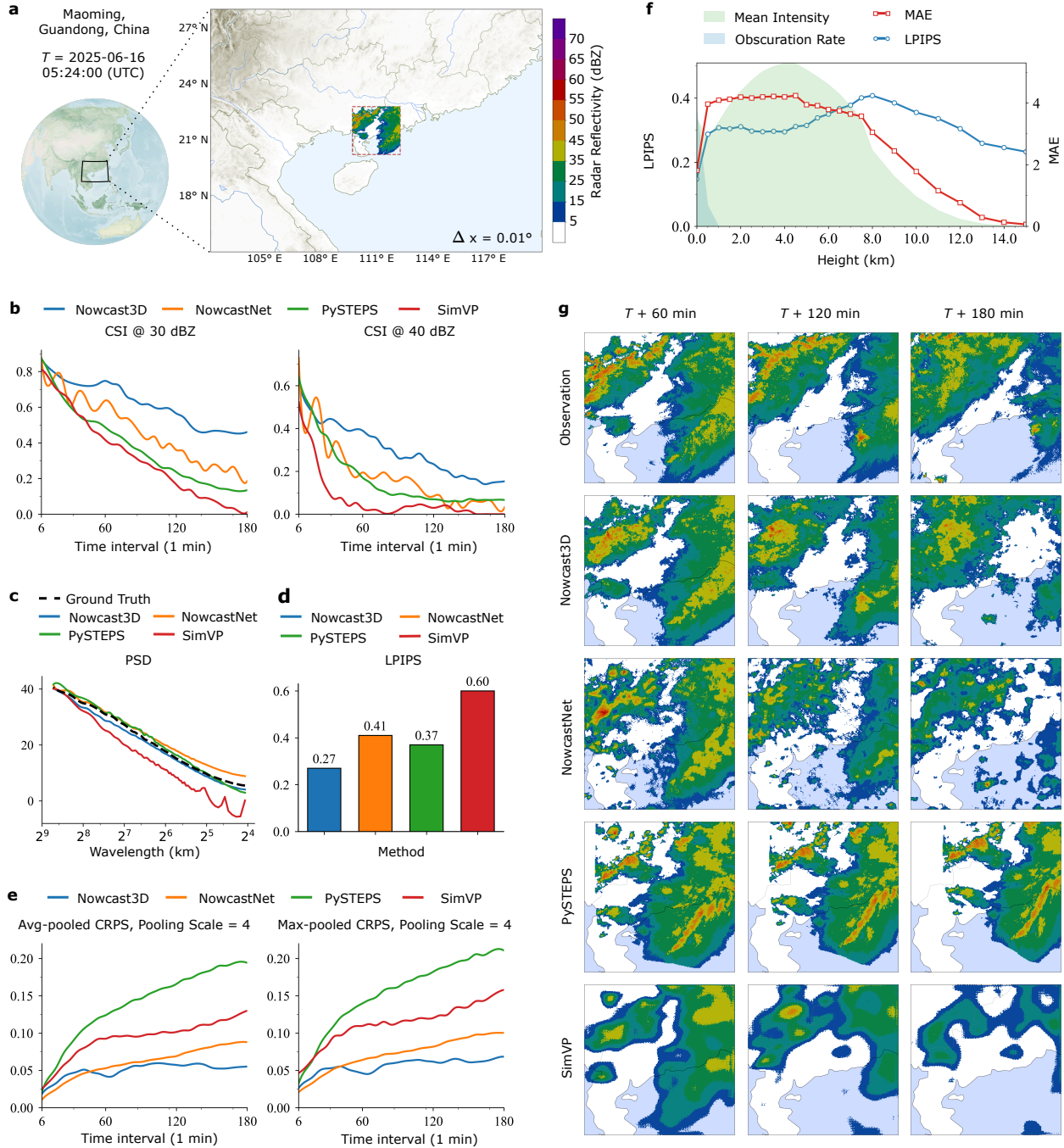


**Figure 3: Generalization of Nowcast3D to high resolution, fine scale forecasting.** **a**, Radar reflectivity over Maoming, Guangdong Province, at the forecast initialization time. The analysis was conducted at  $0.01^\circ$  resolution. **b**, Quantitative forecast skill comparison using the CSI at 30 dBZ and 40 dBZ reflectivity thresholds over the 3 hour forecast horizon. **c**, Analysis of spatial scale fidelity using PSD. Forecast spectra are compared to the observed spectrum (black dashed line). **d**, Perceptual similarity assessment using the LPIPS metric. Lower values indicate better performance. **e**, Probabilistic forecast skill assessed using the CRPS, shown as both average-pooled and max-pooled values. Lower scores indicate better-calibrated ensemble forecasts. **f**, Vertical profiles of forecast error and skill. MAE and LPIPS are plotted as a function of height, overlaid with the mean observed reflectivity and data coverage profiles. **g**, Visual comparison of forecast reflectivity fields from Nowcast3D and baseline models against the observed radar sequence.

cells. The western cell underwent significant expansion, while the eastern cell translated across and eventually exited the forecast domain. The primary challenges were therefore to accurately represent storm morphology under rapid advection and to capture the dynamics of cell growth, which involved large and abrupt changes in reflectivity.

Comparing the predicted spatio-temporal evolution at this high resolution highlights the difficulty models face in forecasting rapidly evolving radar fields (Figure 3g). The baseline models, NowcastNet and SimVP, capture the general eastward trend but fail to reproduce the expansion of the western cell, resulting in spatially fragmented predictions. The parameter free pySTEPS model underestimates the system’s translation speed and does not capture its area growth. In contrast, Nowcast3D demonstrates substantially improved performance, more faithfully capturing both the rapid eastward displacement and the structural expansion of the convective system.

Quantitative analyses confirm these visual assessments of forecast skill. Nowcast3D outperforms all baseline models by a significant margin in the neighborhood CSI, indicating superior accuracy in locating precipitation (Figure 3b). Moreover, evaluations using PSD and the LPIPS show that our forecasts are both more faithful to the observed scale-dependent variability and perceptually more realistic (Figure 3c,d). Crucially, as Nowcast3D generates ensembles, we also evaluated its probabilistic skill. The Continuous Ranked Probability Score (CRPS) [35, 36] demonstrates that Nowcast3D produces better-calibrated forecasts than the ensemble based NowcastNet, indicating a more reliable quantification of uncertainty (Figure 3e).

Leveraging its native 3D architecture, we also evaluated the vertical structure of the forecast (Figure 3f). An analysis of layer wise forecast error reveals that performance is strongest in the lower and upper troposphere, with more modest skill in the mid-levels. This pattern is consistent with the vertical distribution of radar observations, which are often sparser at low altitudes and detect intrinsically weaker reflectivity aloft. A comparison of the 3D layered predictions is presented in Extended Data Figure 3.

## Meteorologist evaluation

To evaluate the predictive performance of different models for extreme precipitation events, we followed the meteorological assessment protocols of DGMR [37] and NowcastNet [1]. To ensure fairness and objectivity, a nationwide open invitation was extended to senior meteorologists across China. Forecasts from the competing models were displayed anonymously and in randomized order to avoid bias.

A total of 160 meteorologists from the China Meteorological Administration and 30 provincial or municipal observatories participated. The demographic distribution of participants is shown in Figure 4a. The experts represented almost all regions of China, except Tibet, Hong Kong, Macao, and Taiwan. Each meteorologist evaluated 23 test cases, randomly sampled from precipitation events that occurred in China. Following the NowcastNet protocol [1], we ran two complementary evaluation modes: post-hoc and prior. In the post-hoc mode, meteorologists ranked model forecasts objectively with access to future ground-truth observations. In the prior mode, they ranked forecasts subjectively using only preceding radar sequences, without access to future outcomes — a setting that mimics real operational nowcasting, where rapid decisions must be made without knowledge of subsequent observations.

The aggregated results appear in Figure 4b. In the post-hoc evaluation, Nowcast3D was the most preferred model in 57% of cases; in the prior evaluation it remained the top choice in 51% of cases. Overall, Nowcast3D received the highest preference among meteorologists — likely because its explicit modeling of three dimensional physical fields and the embedding of physical equations

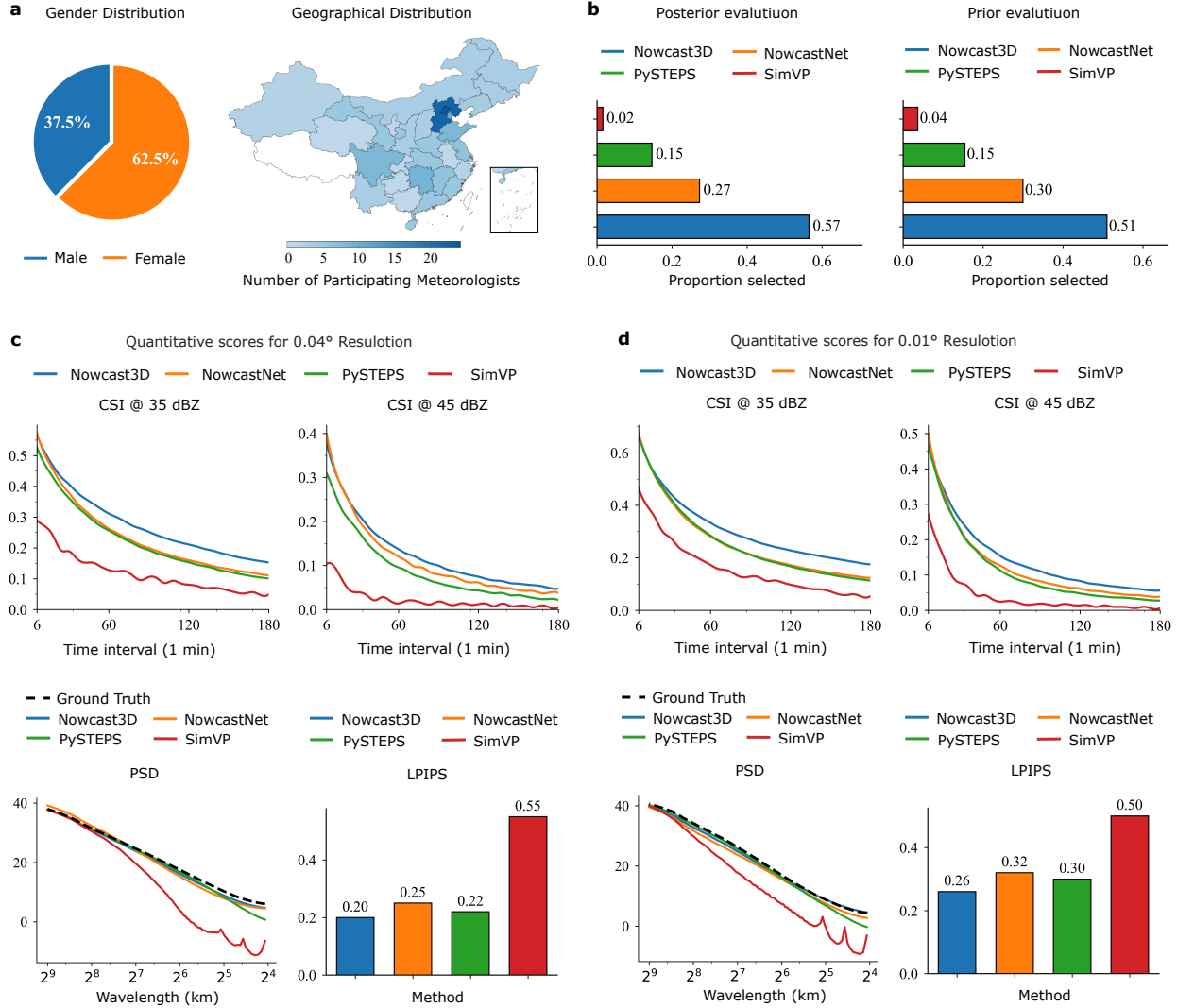


**Figure 4: Aggregate quantitative evaluation of forecast skill.** **a**, Information of participating meteorologists, including gender distribution and regional distribution of their affiliated institutions. **b**, Evaluation of meteorologists’ model preferences across different regions of China. Compared with other competing methods, meteorologists showed a stronger preference for Nowcast3D. **c**, Forecast skill metrics evaluated on the 0.04° resolution test set. The top panels show the CSI as a function of lead time at 35 dBZ and 45 dBZ thresholds. The bottom-left panel shows the power spectral density (PSD) of forecasts compared with the ground truth (black dashed line), and the bottom-right panel shows the mean LPIPS, where lower values indicate better perceptual quality. **d**, The same set of metrics as in **c**, evaluated on the 0.01° resolution test set to assess generalization at finer spatial scales.

enable more accurate capture of 3D radar reflectivity dynamics and, consequently, superior forecasts. Other models, constrained by their inherent 2D formulation, showed limitations in reproducing the realistic spatiotemporal structures of precipitation events.

## Quantitative evaluation

To quantitatively assess forecast skill, we performed a rigorous evaluation using three complementary metrics: the neighbourhood CSI for locational accuracy, PSD for spatial-scale fidelity, and the LPIPS for structural realism. The analysis was performed across the entire test corpus at two

distinct spatial scales: a provincial-level scope at a standard  $0.04^\circ$  resolution, and a more challenging city-level scope at a high  $0.01^\circ$  resolution. This dual-scale approach allowed us to assess both the model’s baseline performance and its generalization capabilities.

At the  $0.04^\circ$  resolution, Nowcast3D demonstrated unambiguous superiority over all baseline models across every performance benchmark (Figure 4c). For both moderate (35 dBZ) and high (45 dBZ) reflectivity thresholds, it achieved the highest CSI scores throughout the 3 hour forecast horizon, indicating an enhanced capability to pinpoint significant precipitation events. The PSD analysis further revealed that forecasts from Nowcast3D most faithfully reproduced the observed power spectrum, signifying a more physically realistic representation of precipitation structures. This was corroborated by the LPIPS metric, on which Nowcast3D obtained the lowest error, confirming the high perceptual and structural fidelity of its predictions.

Crucially, this performance advantage is maintained in the  $0.01^\circ$  resolution evaluation, a more stringent test of the model’s predictive power at finer scales (Figure 4d). The consistent superiority of Nowcast3D across all metrics at this more challenging resolution underscores the robustness of its learned physical representations. Collectively, these results demonstrate that by integrating three dimensional dynamics, Nowcast3D produces forecasts that are more accurate, physically realistic, and perceptually coherent than competing methods, establishing that this advantage is robust across different spatial scales.

## Discussion

Precipitation nowcasting remains a fundamental challenge in atmospheric science, governed by intrinsically stochastic, multiscale processes. While recent progress in data driven methods has improved short range guidance, predictive skill for high impact weather continues to decay rapidly with lead time. This limitation is particularly acute for events where complex vertical structure and microphysical evolution are dominant. Prevailing methods that rely on two dimensional data neglect the vertical dimension, where critical dynamics such as vertical motion and wind shear unfold, thereby limiting their physical fidelity and operational utility in hazardous weather regimes.

Our work introduces a framework that directly confronts these limitations by integrating physics informed dynamics with deep generative modeling on native three dimensional radar volumes. The core innovation is a model that learns to infer and extrapolate key physical drivers directly from sequences of volumetric reflectivity: the three dimensional wind field governing advection, a localized field representing stochastic dispersion, and residual reflectivity evolution driven by unresolved microphysics. The forecast is then advanced using physical principles, enforcing dynamical consistency and allowing the model to produce physically plausible predictions over extended lead times. This physics driven core is coupled with a deep generative model that reconstructs the full conditional distribution of future states, capturing uncertainty in both storm structure and localized intensity. This dual approach yields forecasts that are not only dynamically consistent but also probabilistically reliable, providing essential uncertainty quantification for decision making.

The framework’s performance, however, depends on several factors. First, its accuracy is contingent on the quality, coverage, and scan strategy of the input radar data; issues such as beam attenuation and anomalous propagation remain sources of error. Second, the inference of three dimensional flow from reflectivity is under constrained, particularly in regimes dominated by complex microphysics where phase changes can alter reflectivity without a corresponding change in the velocity field. These limitations define clear avenues for future research. Integrating multi-modal observations, such as Doppler radial velocities, geostationary satellite imagery, and lightning data, could better constrain the inferred wind fields and improve the realism of predicted hydrometeors.

Furthermore, a tighter coupling with numerical weather prediction models, either through data assimilation or as a learned physical prior, could substantially improve forecast skill beyond the nowcasting horizon.

In conclusion, by unifying physics informed dynamics with deep generative modeling on three dimensional data, this work establishes a blueprint for a new generation of nowcasting systems. These models move beyond simple pattern extrapolation to learn representations of the underlying physical processes, resulting in more accurate, reliable, and physically consistent forecasts. The path forward involves enriching this framework by integrating the multi-modal observations and NWP model coupling discussed previously. Pursuing these extensions will be critical in closing the gap towards the reliable, actionable forecasts of high impact weather that are urgently needed today.

## Methods

### Problem statement

We represent the observed 3D radar reflectivity as  $R \in \mathbb{R}^{T \times D \times H \times W}$ , and define the past segment as  $R_{-T_0:0} \in \mathbb{R}^{T_0 \times D \times H \times W}$ . Given  $R_{-T_0:0}$ , our objective is to forecast the future sequence  $R_{1:T}$  through a two-stage hybrid process that combines physics-based deterministic prediction with probabilistic ensemble refinement.

In the physics-driven stage, a physics-learning module  $\Theta$  transforms the historical radar observations into time-varying physical fields:  $X_{1:T} = \Theta(R_{-T_0:0})$ , where  $X_{1:T} \in \mathbb{R}^{T \times C \times D \times H \times W}$  and  $C$  denotes the number of physical quantities governing reflectivity evolution. These inferred fields are incorporated into the governing spatio-temporal equations. The radar reflectivity  $R$  evolves in time according to a partial differential equation  $\partial_t R = \mathcal{F}(R, X)$ , where  $\mathcal{F}$  represents the physical dynamics controlled by  $X$ . Starting from the initial condition  $R(0) = R_0$ , the solution of this equation yields a deterministic forecast  $R_{1:T}^{\text{det}}$ .

In the probabilistic refinement stage, a conditional diffusion model [26, 28] generates a calibrated ensemble. The model  $\Phi$  is conditioned on the context  $c = \{R_{-T_0:0}, R_{1:T}^{\text{det}}\}$ , which contains both the historical radar sequence and the deterministic forecast. Ensemble members are obtained by sampling the learned conditional distribution using different noise realizations  $\epsilon^{(k)}$ , thereby capturing stochastic variability and uncertainty around the physics-consistent prediction.

The overall forecasting process can be summarized by the following equations:

$$\begin{aligned}
 X_{1:T} &= \Theta(R_{-T_0:0}), \quad X_{1:T} \in \mathbb{R}^{T \times C \times D \times H \times W} \quad (\text{map}) \\
 R_{1:T}^{\text{det}} &= \text{Solve}\left(\frac{\partial R}{\partial t} = \mathcal{F}(R, X), R(0) = R_0\right) \quad (\text{PDE solver}) \\
 c &= \{R_{-T_0:0}, R_{1:T}^{\text{det}}\} \quad (\text{conditioning}) \\
 R_{1:T}^{(k)} &= \text{Sample}_{\Phi}(\epsilon^{(k)}, c), \quad k = 1, \dots, K \quad (\text{sampling}) \\
 R_{1:T}^{\text{ens}} &= \{R_{1:T}^{(k)}\}_{k=1}^K \quad (\text{ensemble})
 \end{aligned} \tag{1}$$

### Model Details

**Physics-Informed Forecasting Module.** The deterministic forecast,  $R_{1:T}^{\text{det}}$ , is produced by this module through the numerical integration of a governing partial differential equation. Specifically, we define the physical dynamics  $\mathcal{F}(R, X)$  introduced above with an advection-diffusion-source equa-

tion:

$$\frac{\partial R}{\partial t} = \underbrace{-\mathbf{v} \cdot \nabla R}_{\text{Advection}} + \underbrace{\boldsymbol{\kappa} \nabla^2 R}_{\text{Diffusion}} + \underbrace{s}_{\text{Source}}. \quad (2)$$

This formulation models the evolution of the reflectivity field  $R$  as a composite of three physically distinct processes: large-scale advection by a 3D velocity field  $\mathbf{v}$ ; local anisotropic diffusion governed by the diffusivity tensor  $\boldsymbol{\kappa}$ ; and unresolved dynamics, including microphysical processes, represented by the source term  $s$ . These three time-varying quantities  $(\mathbf{v}, \boldsymbol{\kappa}, s)$  constitute the physical fields  $X_{1:T}$  that are inferred from the input radar sequence  $R_{-T_0:0}$  by the physics-learning module  $\Theta$ . To obtain the deterministic forecast, we solve this governing equation from the initial condition  $R(0) = R_0$  using an operator-splitting scheme, which incorporates the inferred physical fields at each forecast step.

**Neural Parameterization of Physical Fields.** The time-varying physical fields  $X_{1:T} = (\mathbf{v}_{1:T}, \boldsymbol{\kappa}_{1:T}, s_{1:T})$  required to solve Equation (2) are inferred from the input radar sequence by the physics-learning module  $\Theta$ . This module uses a shared encoder-decoder architecture to map the input history  $R_{-T_0:0}$  to the components of  $X$  over the full forecast horizon (Figure 1a). The shared backbone first encodes the input into a latent space-time embedding. This embedding is then processed in parallel by a U-Net [38] branch, capturing local features, and a Transformer [39] branch, modelling long-range dependencies. The fused output from these branches is passed to three distinct decoders that parameterize the physical fields:

$$\begin{aligned} (\varphi_{1:T}, \boldsymbol{\psi}_{1:T}) &= \text{Decoder}_{\text{Motion}}(\text{Backbone}(R_{-T_0:0})) \\ \boldsymbol{\kappa}_{1:T} &= \text{Decoder}_{\text{AnisoBrown}}(\text{Backbone}(R_{-T_0:0})) \\ s_{1:T} &= \text{Decoder}_{\text{Intensity}}(\text{Backbone}(R_{-T_0:0})) \end{aligned} \quad (3)$$

where the full velocity field is reconstructed from the learned scalar potential  $\varphi$  and vector potential  $\boldsymbol{\psi}$  via  $\mathbf{v}_{1:T} = \nabla \varphi_{1:T} + \nabla \times \boldsymbol{\psi}_{1:T}$ . While the backbone feature extractor is shared across all tasks, the three decoders operate with independent parameters, specializing in inferring the dynamics of motion, diffusion, and source terms, respectively (see Supplementary Information for full architectural details).

**Dynamics-Driven Extrapolation.** With the physical fields  $(\mathbf{v}_{1:T}, \boldsymbol{\kappa}_{1:T}, s_{1:T})$  inferred, we evolve the radar field  $R_t$  forward in time by numerically integrating Equation (2). We employ an operator-splitting scheme that decomposes each one-step update into a sequence of advection, diffusion, and source operations. The advection operator,  $\mathcal{A}_{\Delta t}[R_t](x) := R_t(x - \mathbf{v}_t(x)\Delta t)$ , is implemented using a robust semi-Lagrangian scheme. Motivated by the fundamental link between macroscopic diffusion and microscopic random walks [40, 41], the anisotropic diffusion operator  $\mathcal{D}_{\Delta t}$  is implemented stochastically. Its action is defined as an expectation over random displacements,  $\mathcal{D}_{\Delta t}[R_t](x) := \mathbb{E}_{\eta \sim \mathcal{N}(0, 2\boldsymbol{\kappa}_t \Delta t)}[R_t(x + \eta)]$ , and the source term is applied as a final additive correction.

The complete update is expressed compactly by composing these operators:

$$R_{t+1} \approx \mathcal{D}_{\Delta t}[\mathcal{A}_{\Delta t}[R_t]] + s_t \Delta t. \quad (4)$$

In practice, the expectation in the diffusion step is approximated via a Monte-Carlo average over  $M$  samples. This yields the computational update rule for a voxel at location  $x$ :

$$R_{t+1}(x) \approx \frac{1}{M} \sum_{m=1}^M R_t(x - \mathbf{v}_t(x) \Delta t + \eta_t^{(m)}(x)) + s_t(x) \Delta t, \quad (5)$$

where each stochastic displacement  $\eta_t^{(m)}(x)$  is an independent sample from the zero-mean normal distribution  $\mathcal{N}(0, 2\kappa_t(x)\Delta t)$ . Further implementation details are provided in the Supplementary Information.

**Probabilistic Refinement Module.** The probabilistic refinement module implements the sampling process,  $R_{1:T}^{(k)} = \text{Sample}_{\Phi}(\epsilon^{(k)}, c)$ , to generate the ensemble forecast. It is realized as a conditional diffusion model  $\Phi$  that conditions on the context  $c = \{R_{-T_0:0}, R_{1:T}^{\text{det}}\}$ . A key feature of our approach is a dual-branch architecture. Here, a single reverse diffusion process—starting from a Gaussian noise realization  $\epsilon^{(k)}$  and iteratively denoising—produces not one field, but a pair of correlated fields: a full-field structure  $S_{\text{struct}}^{(k)}$  and a residual field  $S_{\text{res}}^{(k)}$ .

This dual output enables the construction of three distinct types of physically meaningful ensemble members from each sample pair:

$$\begin{aligned} S^{(1)} &= S_{\text{struct}} \quad (\text{Full-field forecast}), \\ S^{(2)} &= R_{1:T}^{\text{det}} + S_{\text{res}} \quad (\text{Physics-corrected forecast}), \\ S^{(3)} &= S_{\text{struct}} + \alpha S_{\text{res}} \quad (\text{Hybrid forecast}). \end{aligned} \tag{6}$$

The full predictive ensemble,  $R_{1:T}^{\text{ens}}$ , is constructed by generating  $K$  independent sample pairs  $\{(S_{\text{struct}}^{(k)}, S_{\text{res}}^{(k)})\}_{k=1}^K$  and applying these three strategies to each. This results in a comprehensive ensemble of  $3K$  members, providing a robust characterization of predictive uncertainty:

$$R_{1:T}^{\text{ens}} = \bigcup_{k=1}^K \{S_{\text{struct}}^{(k)}, R_{1:T}^{\text{det}} + S_{\text{res}}^{(k)}, S_{\text{struct}}^{(k)} + \alpha S_{\text{res}}^{(k)}\}. \tag{7}$$

## Model Architecture and Training Protocol

The framework is trained using a sequential, two-stage protocol. First, we train the physics-informed module to learn the deterministic dynamics of precipitation evolution. Its parameters are then frozen, after which the probabilistic module is trained to learn the conditional distribution of forecast errors, conditioned on the deterministic predictions.

**Stage 1: Physics-Informed Deterministic Forecasting.** In this stage, we optimize the parameters of the physics-learning module,  $\Theta$ , comprising its shared backbone (U-Net and Transformer branches) and three distinct decoders. The training objective,  $\mathcal{L}_{\text{phys}}$ , is a composite loss that provides deep supervision by penalizing errors at each step of the physical operator sequence. The total loss is a weighted sum of L1 norms between the intermediate and final predictions and the ground truth,  $R^{\text{truth}}$ , aggregated over the forecast horizon:

$$\mathcal{L}_{\text{phys}} = \sum_{t=0}^{T-1} \left( \lambda_{\text{adv}} \mathcal{L}_{\text{adv}}^{(t)} + \lambda_{\text{diff}} \mathcal{L}_{\text{diff}}^{(t)} + \mathcal{L}_{\text{pred}}^{(t)} \right), \tag{8}$$

where the component losses are defined on the outputs of the advection operator ( $\mathcal{A}_{\Delta t}$ ), the diffusion operator ( $\mathcal{D}_{\Delta t}$ ), and the final source-corrected state:

$$\begin{aligned} \mathcal{L}_{\text{adv}}^{(t)} &= \|\mathcal{A}_{\Delta t}[R_t] - R_{t+1}^{\text{truth}}\|_1, \\ \mathcal{L}_{\text{diff}}^{(t)} &= \|\mathcal{D}_{\Delta t}[\mathcal{A}_{\Delta t}[R_t]] - R_{t+1}^{\text{truth}}\|_1, \\ \mathcal{L}_{\text{pred}}^{(t)} &= \|R_{t+1} - R_{t+1}^{\text{truth}}\|_1. \end{aligned} \tag{9}$$

**Stage 2: Probabilistic Refinement.** With the parameters of  $\Theta$  frozen, we train the probabilistic refinement module. Its dual-branch architecture is explicitly designed to generate the structured field ( $S_{\text{struct}}$ ) and residual field ( $S_{\text{res}}$ ) required for our ensemble construction strategy (Equation (7)). To achieve this, the Structure Generator is trained to learn the distribution of the full ground-truth field, while the Residual Generator learns the distribution of the deterministic forecast error. Both are trained on 2D spatial slices to reduce computational cost. The training objective for each branch is the standard diffusion model loss, which minimizes the mean squared error between the true and predicted noise  $\epsilon$ :

$$\begin{aligned}\mathcal{L}_{\text{struct}} &= \mathbb{E}_{t, R_{\text{truth}}, \epsilon} \|\epsilon - \epsilon_{\theta_{\text{struct}}}(\sqrt{\bar{\alpha}_t} R_{\text{truth}} + \sqrt{1 - \bar{\alpha}_t} \epsilon, t, c)\|_2^2, \\ \mathcal{L}_{\text{res}} &= \mathbb{E}_{t, r, \epsilon} \|\epsilon - \epsilon_{\theta_{\text{res}}}(\sqrt{\bar{\alpha}_t} r + \sqrt{1 - \bar{\alpha}_t} \epsilon, t, c)\|_2^2,\end{aligned}\tag{10}$$

where  $R_{\text{truth}}$  is the 2D ground-truth field,  $r = R_{\text{truth}} - R_{1:T}^{\text{det}}$  is the residual error,  $c$  is the conditioning context, and  $\epsilon \sim \mathcal{N}(0, \mathbf{I})$  is the sampled noise. This training protocol equips the module to generate the correlated field pairs that form the basis of our comprehensive ensemble forecast.

## Experimental Design and Evaluation

**Training Procedure.** The framework was trained in a distributed data-parallel configuration across four NVIDIA A800 GPUs using the NCCL backend. Parameters were optimized using the Adam optimizer [42] with an initial learning rate of  $10^{-3}$ , which was decayed by a factor of 0.8 every 5 epochs. All models were trained for 100 epochs, and we selected the checkpoint with the best performance on a held-out validation set for all subsequent evaluations.

**Datasets.** The model was trained on radar observations from Southern China (110.0°–120.23°E, 23.97°–34.2°N) recorded in 2024, a region selected for its diverse convective weather regimes. This data has a native horizontal resolution of 0.01° and 24 vertical layers spanning from 0.5 to 16 km altitude. To assess generalization, we used two independent test sets. The coarse-resolution evaluation was performed on data from Northern China (110.0°–120.23°E, 33.97°–44.2°N) from the first half of 2025. The fine-resolution evaluation used data from the Guangdong region, an area with no geographical overlap with the training data, known for extreme typhoon-induced precipitation.

**Evaluation Protocols.** We evaluated model performance at two spatial resolutions: 0.04° (coarse) and 0.01° (fine), processing 256×256-pixel input patches in both cases. These settings correspond to a 10.24°×10.24° physical domain for large-scale forecasting and a 2.56°×2.56° domain for high-resolution hazard warnings, respectively. The main high-resolution results reported herein were obtained after fine-tuning the model on a portion of the 2024 Guangdong data; for completeness, results from direct inference without fine-tuning are provided in the Supplementary Information.

**Evaluation Metrics.** We assess forecast skill using a suite of three complementary metrics. (1) Detection and localization skill is quantified using the Critical Success Index (CSI) at meteorologically significant reflectivity thresholds (20, 30, 40, and 50 dBZ). (2) Perceptual and structural fidelity is evaluated using the Learned Perceptual Image Patch Similarity (LPIPS) metric with a pre-trained AlexNet backbone, which aligns well with human visual judgment. (3) Scale-dependent realism is diagnosed via Power Spectral Density (PSD) analysis. By radially averaging the 2D power spectrum, we obtain a 1D spectrum as a function of wavelength, enabling a direct comparison of the energy distribution from convective to mesoscale ranges between forecasts and ground truth.

**Validation of Inferred Wind Fields.** To validate the physical realism of the velocity field  $\mathbf{v}$  inferred by Nowcast3D (Equation 3), we performed a quantitative comparison against observations from wind profiler radar. This required a two-step post-processing protocol (Extended Data Figure 5a). First, the model’s native output, grid-cell displacement per 6-minute interval, was converted to degrees. Second, these values were transformed into physical velocity components (in m/s) using latitude-dependent scaling to account for spherical geometry. As the profiler sites do not align perfectly with Nowcast3D’s grid points, we developed a spatio-temporal matching method. For each observation, we defined a horizontal search radius and a vertical tolerance window (Extended Data Figure 5b,c). The corresponding model prediction was computed by averaging all grid-point values within this 3D cylinder. Using this matched dataset, we evaluated two aspects of performance over the forecast horizon. The Pearson correlation coefficient between the predicted and observed wind speeds (Extended Data Figure 5d), and the mean absolute error (MAE) of the wind direction (Extended Data Figure 5e).

## Data availability

The three dimensional radar data used in this study to support the training of nowcasting models in China were provided by the China Meteorological Administration (CMA). These data are available from the authors upon reasonable request and with permission from the CMA. A demonstration dataset used in this paper is publicly accessible at <https://github.com/Huaguan-Chen/Nowcast3D>.

## Code availability

All the source codes to reproduce the results in this study are available in the GitHub repository at <https://github.com/Huaguan-Chen/Nowcast3D>.

## References

- [1] Yuchen Zhang, Mingsheng Long, Kaiyuan Chen, Lanxiang Xing, Ronghua Jin, Michael I Jordan, and Jianmin Wang. Skilful nowcasting of extreme precipitation with NowcastNet. *Nature*, 619(7970):526–532, 2023.
- [2] Mariusz Starzec, Gretchen L Mullendore, and Paul A Kucera. Using radar reflectivity to evaluate the vertical structure of forecast convection. *Journal of Applied Meteorology and Climatology*, 57(12):2835–2849, 2018.
- [3] Gabriele Franch, Valerio Maggio, Luca Coviello, Marta Pendesini, Giuseppe Jurman, and Cesare Furlanello. TAASRAD19, a high-resolution weather radar reflectivity dataset for precipitation nowcasting. *Scientific Data*, 7(1):234, 2020.
- [4] Shigenori Otsuka, Gulanbaier Tuerhong, Ryota Kikuchi, Yoshikazu Kitano, Yusuke Taniguchi, Juan Jose Ruiz, Shinsuke Satoh, Tomoo Ushio, and Takemasa Miyoshi. Precipitation nowcasting with three-dimensional space-time extrapolation of dense and frequent phased-array weather radar observations. *Weather and Forecasting*, 31(1):329–340, 2016.
- [5] Matthias Steiner, Robert A Houze Jr, and Sandra E Yuter. Climatological characterization of three-dimensional storm structure from operational radar and rain gauge data.

- [6] Michael I Biggerstaff and Steven A Listemaa. An improved scheme for convective/stratiform echo classification using radar reflectivity. *Journal of Applied Meteorology and Climatology*, 39(12):2129–2150, 2000.
- [7] Juanzhen Sun, Ming Xue, James W Wilson, Isztar Zawadzki, Sue P Ballard, Jeanette Onvlee-Hooimeyer, Paul Joe, Dale M Barker, Ping-Wah Li, Brian Golding, et al. Use of NWP for nowcasting convective precipitation: Recent progress and challenges. *Bulletin of the American Meteorological Society*, 95(3):409–426, 2014.
- [8] Kaifeng Bi, Lingxi Xie, Hengheng Zhang, Xin Chen, Xiaotao Gu, and Qi Tian. Accurate medium-range global weather forecasting with 3D neural networks. *Nature*, 619(7970):533–538, 2023.
- [9] Remi Lam, Alvaro Sanchez-Gonzalez, Matthew Willson, Peter Wirnsberger, Meire Fortunato, Ferran Alet, Suman Ravuri, Timo Ewalds, Zach Eaton-Rosen, Weihua Hu, et al. Learning skillful medium-range global weather forecasting. *Science*, 382(6677):1416–1421, 2023.
- [10] Dmitrii Kochkov, Janni Yuval, Ian Langmore, Peter Norgaard, Jamie Smith, Griffin Mooers, Milan Klöwer, James Lottes, Stephan Rasp, Peter Düben, et al. Neural general circulation models for weather and climate. *Nature*, 632(8027):1060–1066, 2024.
- [11] Cristian Bodnar, Wessel P Bruinsma, Ana Lucic, Megan Stanley, Anna Allen, Johannes Brandstetter, Patrick Garvan, Maik Riechert, Jonathan A Weyn, Haiyu Dong, et al. A foundation model for the Earth system. *Nature*, pages 1–8, 2025.
- [12] Xiuyu Sun, Xiaohui Zhong, Xiaoze Xu, Yuanqing Huang, Hao Li, J David Neelin, Deliang Chen, Jie Feng, Wei Han, Libo Wu, et al. A data-to-forecast machine learning system for global weather. *Nature Communications*, 16(1):6658, 2025.
- [13] Yingzhe Cui, Ruohan Wu, Xiang Zhang, Ziqi Zhu, Bo Liu, Jun Shi, Junshi Chen, Hailong Liu, Shenghui Zhou, Liang Su, et al. Forecasting the eddying ocean with a deep neural network. *Nature Communications*, 16(1):2268, 2025.
- [14] Anna Allen, Stratis Markou, Will Tebbutt, James Requeima, Wessel P Bruinsma, Tom R Andersson, Michael Herzog, Nicholas D Lane, Matthew Chantry, J Scott Hosking, et al. End-to-end data-driven weather prediction. *Nature*, 641(8065):1172–1179, 2025.
- [15] Seppo Pulkkinen, Daniele Nerini, Andrés A Pérez Hortal, Carlos Velasco-Forero, Alan Seed, Urs Germann, and Loris Foresti. Pysteps: An open-source Python library for probabilistic precipitation nowcasting (v1. 0). *Geoscientific Model Development*, 12(10):4185–4219, 2019.
- [16] Xingjian Shi, Zhoung Chen, Hao Wang, Dit-Yan Yeung, Wai-Kin Wong, and Wang-chun Woo. Convolutional LSTM network: A machine learning approach for precipitation nowcasting. In *Advances in Neural Information Processing Systems*, volume 28, 2015.
- [17] Yunbo Wang, Mingsheng Long, Jianmin Wang, Zhifeng Gao, and Philip S Yu. PredRNN: Recurrent neural networks for predictive learning using spatiotemporal LSTMs. In *Advances in Neural Information Processing Systems*, pages 879–888, 2017.
- [18] Zhihan Gao, Xingjian Shi, Hao Wang, Yi Zhu, Yuyang Wang, Mu Li, and Dit-Yan Yeung. Earthformer: Exploring space-time transformers for earth system forecasting. In *Advances in Neural Information Processing Systems*, pages 25390–25403, 2022.

- [19] Zhangyang Gao, Cheng Tan, Lirong Wu, and Stan Z. Li. Simvp: Simpler yet better video prediction. In *Proceedings of the IEEE/CVF Conference on Computer Vision and Pattern Recognition*, pages 3170–3180, June 2022.
- [20] Lasse Espeholt, Shreya Agrawal, Casper Sønderby, Manoj Kumar, Jonathan Heek, Carla Bromberg, Cenk Gazen, Rob Carver, Marcin Andrychowicz, Jason Hickey, et al. Deep learning for twelve hour precipitation forecasts. *Nature Communications*, 13(1):5145, 2022.
- [21] Puja Das, August Posch, Nathan Barber, Michael Hicks, Kate Duffy, Thomas Vandal, Debjani Singh, Katie van Werkhoven, and Auroop R Ganguly. Hybrid physics-AI outperforms numerical weather prediction for extreme precipitation nowcasting. *npj Climate and Atmospheric Science*, 7(1):282, 2024.
- [22] H. Helmholtz. Über integrale der hydrodynamischen gleichungen, welche den wirbelbewegungen entsprechen. *Journal für die reine und angewandte Mathematik*, 55:25–55, 1858.
- [23] Jie Cao, Lingkun Ran, and Na Li. An application of the Helmholtz theorem in extracting the externally induced deformation field from the total wind field in a limited domain. *Monthly Weather Review*, 142(5):2060–2066, 2014.
- [24] Lanxiang Xing, Haixu Wu, Yuezhou Ma, Jianmin Wang, and Mingsheng Long. Helmfuid: Learning helmholtz dynamics for interpretable fluid prediction. In *International Conference on Machine Learning*, 2024.
- [25] Andrew Staniforth and Jean Côté. Semi-Lagrangian integration schemes for atmospheric models—A review. *Monthly Weather Review*, 119(9):2206–2223, 1991.
- [26] Jonathan Ho, Ajay Jain, and Pieter Abbeel. Denoising diffusion probabilistic models. In *Advances in Neural Information Processing Systems*, volume 33, pages 6840–6851, 2020.
- [27] Jiaming Song, Chenlin Meng, and Stefano Ermon. Denoising Diffusion Implicit Models. In *9th International Conference on Learning Representations*, 2021.
- [28] Demin Yu, Xutao Li, Yunming Ye, Baoquan Zhang, Chuyao Luo, Kuai Dai, Rui Wang, and Xunlai Chen. Diffcast: A unified framework via residual diffusion for precipitation nowcasting. In *Proceedings of the IEEE/CVF Conference on Computer Vision and Pattern Recognition*, pages 27758–27767, 2024.
- [29] Ilan Price, Alvaro Sanchez-Gonzalez, Ferran Alet, Tom R Andersson, Andrew El-Kadi, Dominic Masters, Timo Ewalds, Jacklynn Stott, Shakir Mohamed, Peter Battaglia, et al. Probabilistic weather forecasting with machine learning. *Nature*, 637(8044):84–90, 2025.
- [30] Lizao Li, Robert Carver, Ignacio Lopez-Gomez, Fei Sha, and John Anderson. Generative emulation of weather forecast ensembles with diffusion models. *Science Advances*, 10(13):eadk4489, 2024.
- [31] Fabio Sigrist, Hans R Künsch, and Werner A Stahel. Stochastic partial differential equation based modelling of large space–time data sets. *Journal of the Royal Statistical Society Series B: Statistical Methodology*, 77(1):3–33, 2015.
- [32] Ian T Jolliffe and David B Stephenson. *Forecast verification: a practitioner’s guide in atmospheric science*. John Wiley & Sons, 2011.

- [33] S Sinclair and GGS Pegram. Empirical Mode Decomposition in 2-D space and time: a tool for space-time rainfall analysis and nowcasting. *Hydrology and Earth System Sciences*, 9(3):127–137, 2005.
- [34] Richard Zhang, Phillip Isola, Alexei A Efros, Eli Shechtman, and Oliver Wang. The unreasonable effectiveness of deep features as a perceptual metric. In *Proceedings of the IEEE/CVF Conference on Computer Vision and Pattern Recognition*, pages 586–595, 2018.
- [35] James E Matheson and Robert L Winkler. Scoring rules for continuous probability distributions. *Management Science*, 22(10):1087–1096, 1976.
- [36] Hans Hersbach. Decomposition of the continuous ranked probability score for ensemble prediction systems. *Weather and Forecasting*, 15(5):559–570, 2000.
- [37] Suman Ravuri, Karel Lenc, Matthew Willson, Dmitry Kangin, Remi Lam, Piotr Mirowski, Megan Fitzsimons, Maria Athanassiadou, Sheleem Kashem, Sam Madge, et al. Skilful precipitation nowcasting using deep generative models of radar. *Nature*, 597(7878):672–677, 2021.
- [38] Olaf Ronneberger, Philipp Fischer, and Thomas Brox. U-Net: Convolutional Networks for Biomedical Image Segmentation. In *International Conference on Medical Image Computing and Computer Assisted Intervention*, pages 234–241. Springer, 2015.
- [39] Ashish Vaswani, Noam Shazeer, Niki Parmar, Jakob Uszkoreit, Llion Jones, Aidan N Gomez, Łukasz Kaiser, and Illia Polosukhin. Attention Is All You Need. *Advances in Neural Information Processing Systems*, 30, 2017.
- [40] Albert Einstein. Über die von der molekularkinetischen Theorie der Wärme geforderte Bewegung von in ruhenden Flüssigkeiten suspendierten Teilchen. *Annalen der Physik*, 4, 1905.
- [41] Sydney Chapman and Thomas George Cowling. *The mathematical theory of non-uniform gases: an account of the kinetic theory of viscosity, thermal conduction and diffusion in gases*. Cambridge University Press, 1990.
- [42] Diederik P Kingma. Adam: A method for stochastic optimization. *arXiv preprint arXiv:1412.6980*, 2014.

## Acknowledgement

The work is supported by the National Natural Science Foundation of China (No. 62276269, No. 92270118) and the Beijing Natural Science Foundation (No. 1232009). We sincerely thank Professor Xiaoding Yu, for his important contribution to the expert evaluation process. We also extend our heartfelt thanks to the 160 anonymous meteorologists who participated in the meteorologist evaluation.

## Author contributions

H.S. (Hao Sun) and W.H. organized and led the project. H.S. (Hao Sun), W.H., and H.C. explored and designed the model and methodology. H.C. developed the Nowcast3D framework,

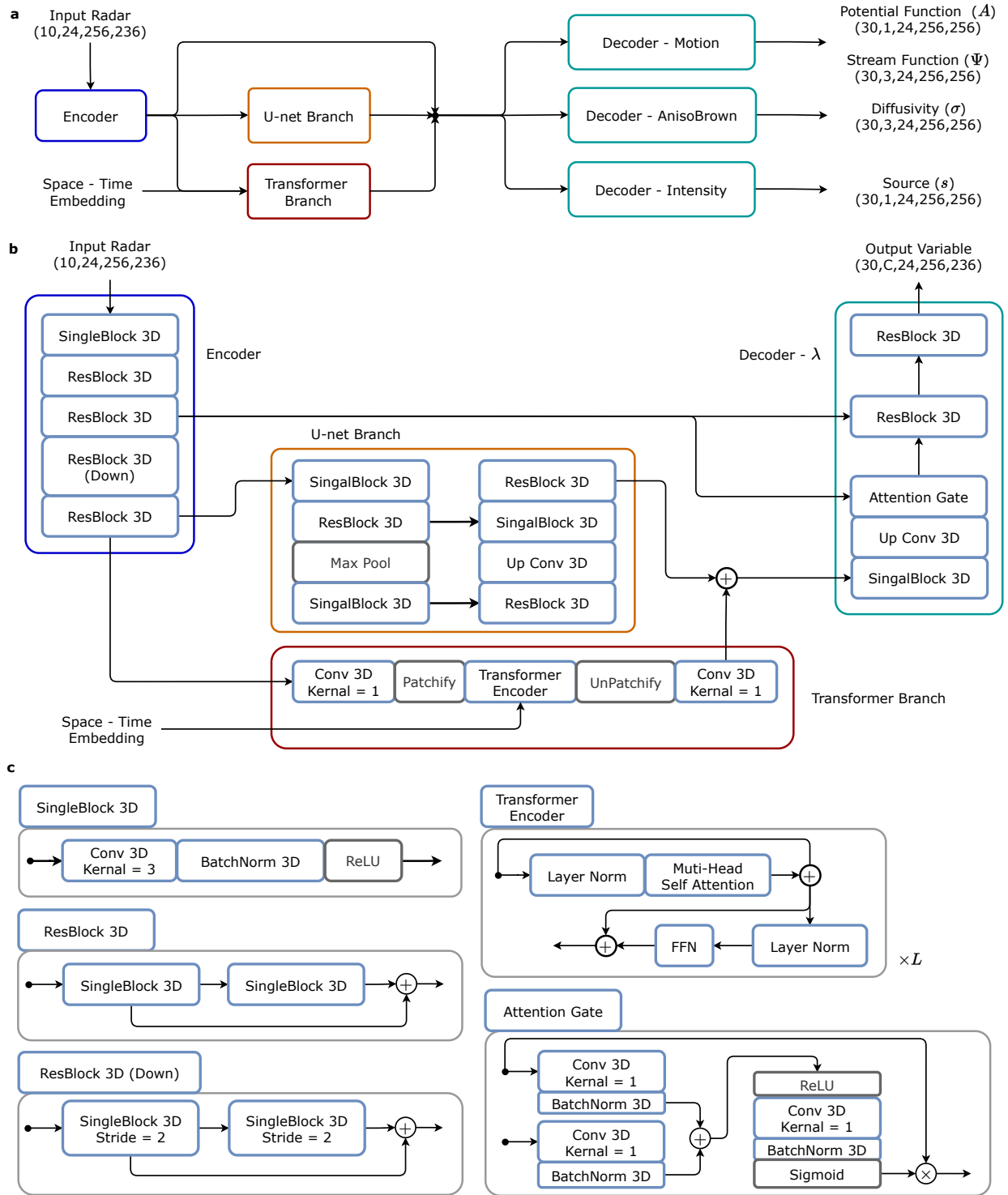
including model architecture, training, and fine-tuning. H.S. (Haofei Sun), Y.Y., and H.C. collected and processed the radar data, while X.S. provided the wind profiler radar data. J.T. and H.C. conducted case studies and analyzed the results. N.L. contributed to the preliminary development and conceptualization of the study. H.S. (Hao Sun) and W.H. supervised all aspects of the project. All authors participated in the writing and revision of the manuscript.

## Corresponding authors

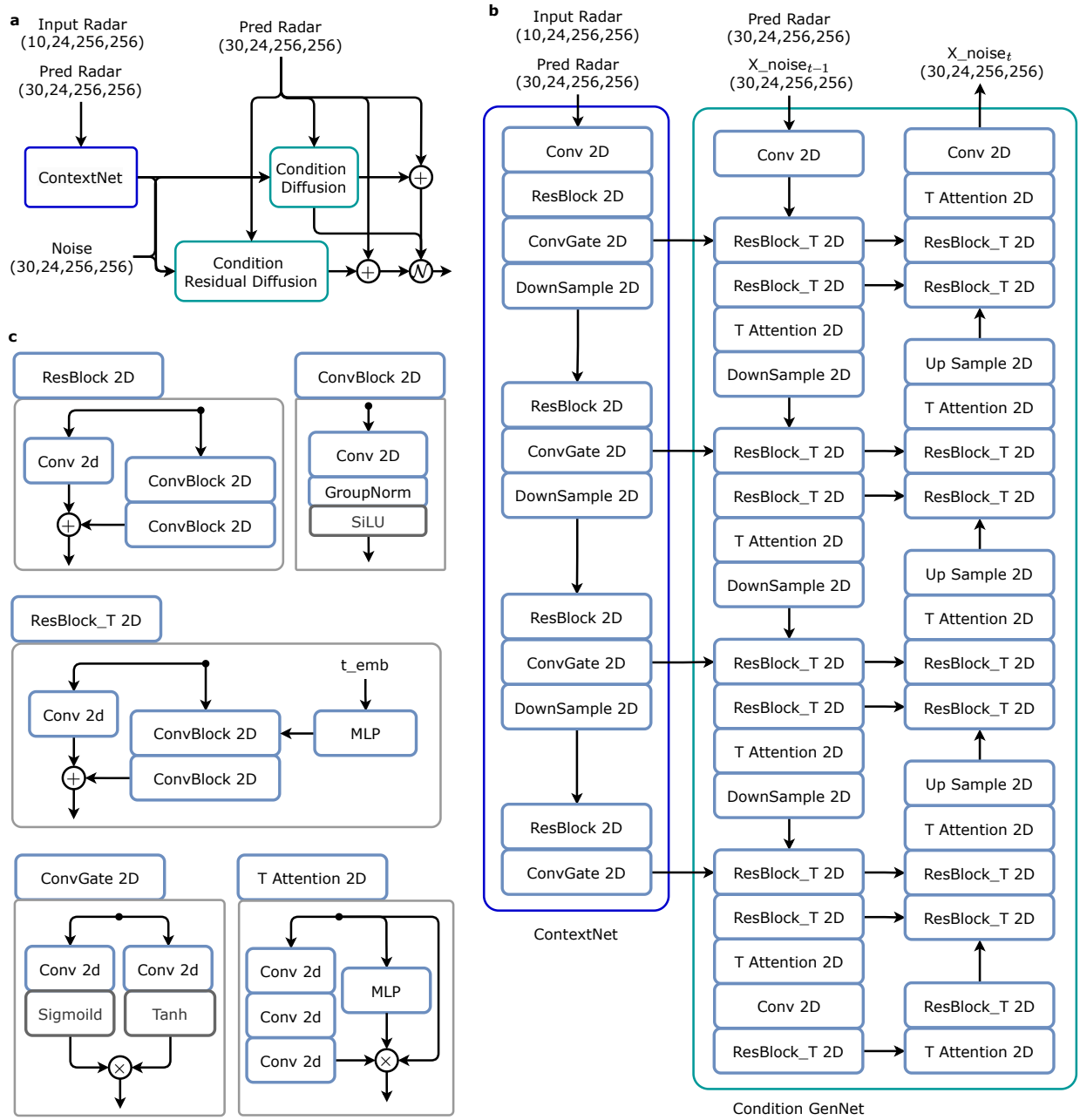
Wei Han ([hanwei@cma.gov.cn](mailto:hanwei@cma.gov.cn)) and Hao Sun ([haosun@ruc.edu.cn](mailto:haosun@ruc.edu.cn)).

## Competing interests

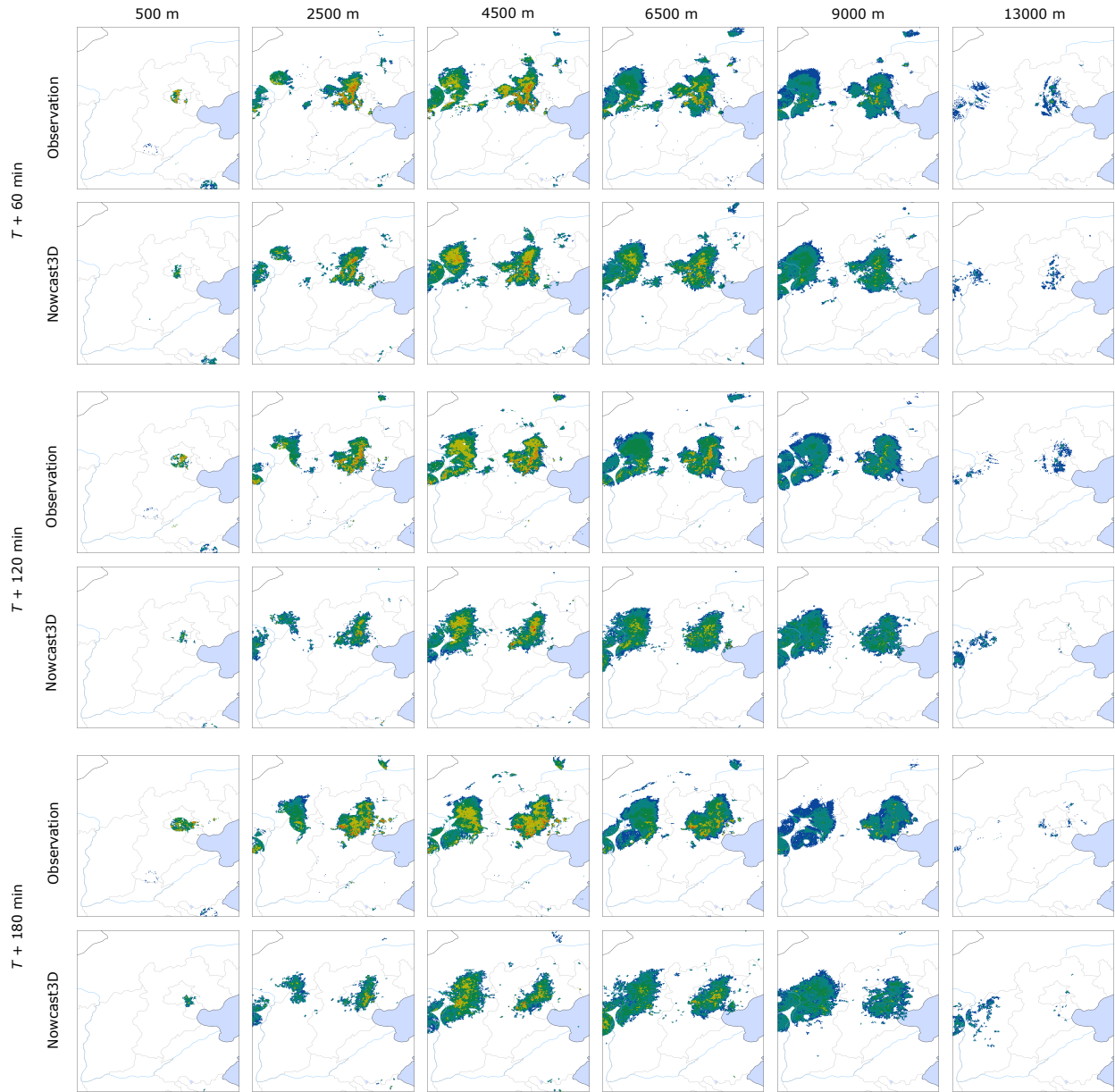
The authors declare no competing interests.



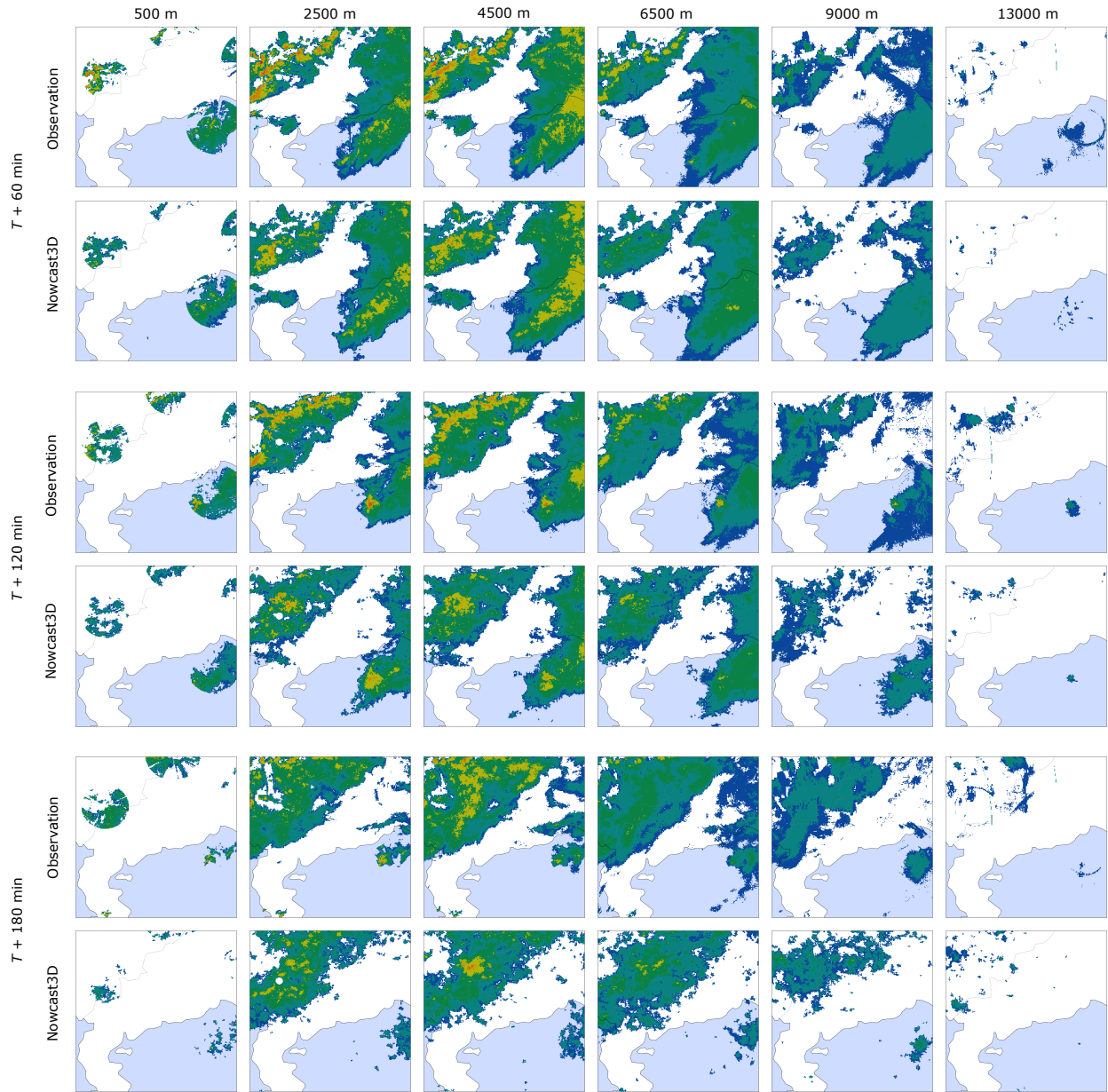
**Extended Data Figure 1: Detailed illustration of the model architecture.** **a**, An overview of the entire model, showing how the Encoder, U-net Branch, Transformer Branch, and multiple Decoders work in concert to process the input radar data and generate predictions for physical quantities. **b**, The detailed architecture of the core forecasting model, providing an in-depth look at the specific layers and connections within the Encoder, U-net Branch, Transformer Branch, and the Decoder. **c**, Schematics of the fundamental building blocks used in the model.



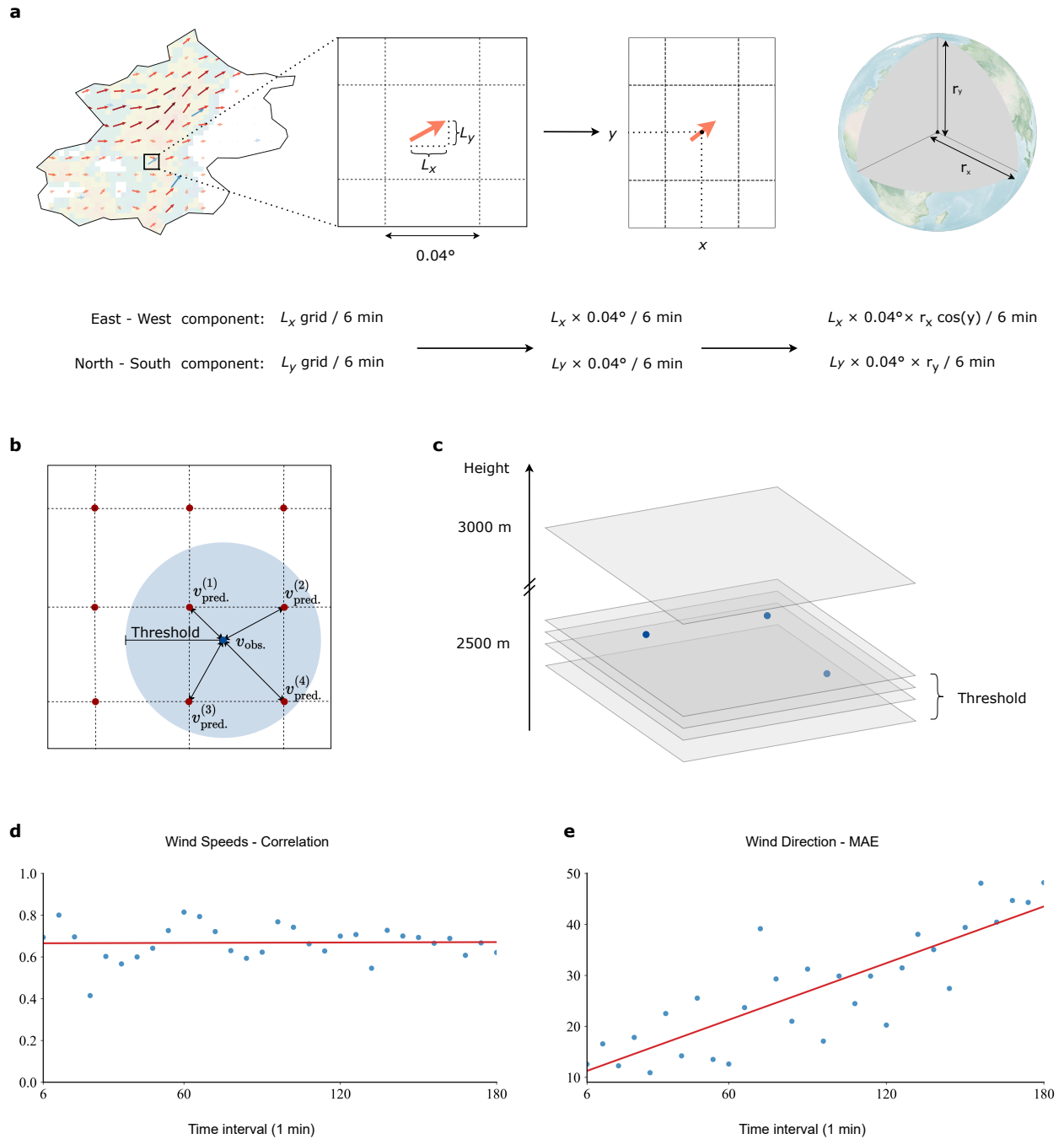
**Extended Data Figure 2: Architectural diagram of the conditional diffusion model.** **a**, An overview of the model, illustrating the conditional residual diffusion process. The ContextNet extracts conditions from the input and an initial prediction, which then guide the diffusion process to refine the final prediction. **b**, The detailed architectures of the ContextNet and the Condition GenNet. The ContextNet acts as an encoder to extract contextual features. The Condition GenNet, which is the core U-Net of the diffusion model, integrates conditioning from the ContextNet and timestep embeddings to predict the noise through multiple levels of down-sampling, up-sampling, and attention mechanisms. **c**, The fundamental building blocks used in the model.



**Extended Data Figure 3: 3D Layered Comparison** This figure corresponds to the layered prediction map in Figure 2. We show a comparison between our prediction results and the ground truth at a specific vertical height. The 500m observation exhibits circular features due to the limitations of the radar detection range, which appears as an overlap of multiple observation circles at low altitudes.



**Extended Data Figure 4: 3D Layered Comparison** This figure corresponds to the layered prediction map in Figure 3. We show a comparison between our prediction results and the ground truth at a specific vertical height. The 500m observation exhibits circular features due to the limitations of the radar detection range, which appears as an overlap of multiple observation circles at low altitudes.



**Extended Data Figure 5: Wind Field Calculation and Evaluation Methodology.** **a**, Schematic of the calculation process from gridded data to the site-specific wind field. **b**, Spatial averaging method for evaluation: Since observation sites do not align perfectly with grid points, we define a circular area with a radius of Threshold around each site. The predicted values within this circle are averaged for comparison with the site's observation. **c**, Vertical averaging method for evaluation: As observations may not match the exact vertical levels of the predictions, we average all observations within a vertical range of  $\pm \text{Threshold} / 2$  from a specific height for comparison. **d**, Temporal evolution of the correlation coefficient between predicted and observed wind speeds. **e**, Temporal evolution of the mean absolute error (or another error metric) in wind direction between predicted and observed fields.